


 Cite this: *RSC Adv.*, 2020, **10**, 26288

 Received 30th May 2020
 Accepted 7th July 2020

DOI: 10.1039/d0ra04776g

rsc.li/rsc-advances

Blackbody emission from CaF₂ and ZrO₂ nanosized dielectric particles doped with Er³⁺ ions

 P. A. Ryabochkina,^a S. A. Khrushchalina,^a I. A. Yurlov,^a A. V. Egorysheva,^b
 A. V. Atanova,^c V. O. Veselova^c and V. M. Kyashkin^a

We studied the features of the appearance of broadband “white” emission in CaF₂-*x* mol% ErF₃ and ZrO₂-*x* mol% Er₂O₃ (*x* = 0–25) nanosized dielectric particles upon their excitation by intense laser radiation with λ_{exc} = 1550 nm. Comparison of the results of this study with the results obtained previously for other materials doped with Er³⁺ ions confirmed the thermal nature of the observed emission and made it possible to identify the main factors affecting its occurrence. These include the band gap of the material and the presence of defects in its structure. A method of applying the effect in dermatology is proposed.

1. Introduction

Nanoscale materials have long attracted the interest of researchers due to their unique properties, which often differ from the properties of bulk compounds of similar compositions. A vivid example is the appearance of broadband “white” emission (BBWE) in nanoscale dielectric materials when they are excited by intense laser radiation.^{1–14} In most cases, this emission was observed in compounds doped with rare-earth (RE) ions upon excitation into the absorption band of these ions. An analysis of these publications indicates that there are different points of view on the nature of the observed phenomenon and the processes responsible for it. If we generalize the researchers’ opinions regarding the physical nature of this emission, we can conditionally divide them into two groups. The first group of researchers believes that the observed emission is inherently thermal (blackbody).^{1,5,11–14} According to the second group of opinions, it represents luminescence and is not associated with sample heating.^{2,3} For example, the authors of^{1,5} attribute the thermal nature to the BBWE observed when the nanosized particles of Y₂O₃:Yb,Er are excited into the absorption band of Yb³⁺ ions. At the same time, broadband emission (BBE) in the visible spectral region, which arises upon excitation of the ²F_{5/2} level of Yb³⁺ ions of LiYbP₄O₁₂:Er nanopowders, is explained by charge transfer luminescence of Yb³⁺ ions.^{2,3}

In our own studies,⁷ we demonstrated that the BBWE arising in Y_{1–*x*}Er_{*x*}PO₄ (*x* = 0–1) nanosized dielectric particles

under laser excitation with λ_{exc} = 970 nm, is thermal. Studies of the features of similar phenomenon in Y_(1–*x*)Er_{*x*}VO₄ and La_{1–*x*}Pr_{*x*}Ga_{0.5}Sb_{1.5}O₆ (*x* = 0–1) nanopowders upon their excitation into the absorption bands of Er³⁺ and Pr³⁺ ions^{8,9} also confirmed its thermal nature. The appearance of BBE in the visible spectral range in the compounds studied by us is a result of their strong heating under the impact of intense laser radiation. In our opinion, such a significant heating of the samples is resulted from the interaction of electrons in the conduction band with phonons of the crystal lattice. The transition of electrons to the conduction band is due to the interaction of excited RE ions with each other and with defects in the crystal structure, a significant amount of which are concentrated in the surface layers of nanoscale particles due to uncompensated bonds in many atoms.

According to the mechanism we proposed, in addition to the excitation power density and the concentration of RE ions, the appearance of BBWE in various matrices^{7–9,14} should be significantly affected by their band gap (*E*_g), the RE ion absorption value at the excitation wavelength, as well as the presence of structure defects. To clarify proposed mechanism and to identify which of these parameters is dominant, it is necessary to study the features of the BBWE appearance in various nanoscale dielectric materials with RE ions, in which these parameters differ significantly.

The study of Y_{1–*x*}Er_{*x*}PO₄ and Y_(1–*x*)Er_{*x*}VO₄ nanoparticles (*x* = 0–1) with a close crystal structure but different band gap (*E*_g = 8.6–9.2 eV (ref. 15 and 16) and 3.4–3.8 eV (ref. 17 and 18), respectively) revealed differences in conditions necessary for the BBWE appearance in them.⁸ For this reason, one of the criteria for choosing compounds for the present study was the value of their band gap, which should differ from values for the materials we have already studied. The next criterion was

^aOgarev Mordovia State University, Saransk 430005, Republic of Mordovia, Russia.
 E-mail: ryabochkina@freemail.mrsu.ru

^bKurnakov Institute of General and Inorganic Chemistry, Russian Academy of Sciences, Leninskii pr. 31, Moscow, 119991, Russia

^cFSRC “Crystallography and Photonics” RAS, Moscow, Russia



the presence of defects in the structure, which would be confirmed experimentally.

Compounds $\text{CaF}_{2-x} \text{ mol\% ErF}_3$ and $\text{ZrO}_{2-x} \text{ mol\% Er}_2\text{O}_3$ ($x = 0-25$) satisfy the proposed criteria, are characterized by the same type of crystal structure, different band gap and have a number of features. Compounds of the $\text{CaF}_2\text{-ReF}_3$ type belong to the structural type of fluorite with a cubic crystal lattice and are wide-gap dielectrics with $E_g = 12 \text{ eV}$.¹⁹ A characteristic feature of such materials is their tendency to form clusters of RE ions at their concentrations of 0.1 at% and higher.^{20,21} At high concentrations of RE ions, the percolation effect is observed for these compounds,^{22,23} which consists in the interaction of clusters with each other. It should also be noted that in most studies, BBWE was detected in oxide nanosized particles doped with RE under laser excitation.^{1-9,11,13,14,24-26} To date, we have found only one such study for fluoride nanosized particles (for LiYbF_4 compounds).²⁶ However, studies on the occurrence of BBE in $\text{CaF}_{2-x} \text{ mol\% ReF}_3$ compounds were not carried out.

$\text{ZrO}_2\text{-M}_2\text{O}_3$ solid solutions (where $M = \text{Y, RE ions}$) are also cubic and are characterized by $E_g = 4.6-5.8 \text{ eV}$ ($x = 8-9.5 \text{ mol\%}$).²⁷⁻³⁰ The features of these compounds are their low thermal conductivity and the presence of defects in the structure (oxygen vacancies) due to heterovalent substitution of Zr^{4+} ions with Y^{3+} or Re^{3+} ions. BBE in the $\text{ZrO}_2\text{-Y}_2\text{O}_3\text{-Yb}_2\text{O}_3\text{-Tm}_2\text{O}_3$ (YSZ:Tm,Yb), $\text{ZrO}_2\text{-Yb}_2\text{O}_3$ and $\text{Y}_{3.93}\text{Yb}_{0.07}\text{Zr}_3\text{O}_{12}$ compounds and the prospects for its practical application in photovoltaics were reported in ref. 11, 12 and 31. However, the physical mechanisms leading to the occurrence of this emission are not presented in the above papers, except that the authors of^{12,31} attribute its occurrence to multiphonon relaxation. A deeper understanding of the physical processes causing the described phenomenon will expand the scope of its application, and will also be of fundamental importance.

Thus, summarizing the currently available experimental facts about BBWE in nanoscale dielectric particles with RE ions when they are excited by intense laser radiation into the absorption bands of these ions, we can state the ambiguity of views on the nature of its occurrence and the expediency of further studies in this direction.

In accordance with this, the aim of this work was to study the BBWE regularities in $\text{CaF}_{2-x} \text{ mol\% ErF}_3$ and $\text{ZrO}_{2-x} \text{ mol\% Er}_2\text{O}_3$ nanoparticles upon their excitation by laser radiation with $\lambda_{\text{exc}} = 1550 \text{ nm}$. It was also interesting to conduct a comparative analysis of the obtained results with results for $\text{Y}_{1-x}\text{Er}_x\text{PO}_4$ and $\text{Y}_{1-x}\text{Er}_x\text{VO}_4$ ($x = 0-1$) to clarify the appearance mechanism of the BBWE in nanoscale dielectric particles with RE ions and to identify the most important factors affecting its occurrence.

2. Experimental section

Nanosized $\text{CaF}_{2-x} \text{ mol\% ErF}_3$ ($x = 5, 10, 15, 25$) crystalline powders of fluorite structure were obtained by chemical coprecipitation according to the reaction:



As starting compounds for the preparation of samples, we used CaCl_2 (Aldrich, 99.9% purity), $\text{ErCl}_3 \cdot 6\text{H}_2\text{O}$ (Aldrich, 99.9% purity), NH_4F (Vecton, 99.9% purity) and deionized water. The mass of reagents was determined to the third decimal place. 25 ml of an initial aqueous solution with a concentration of 0.02 M containing calcium chloride ions and an alloying impurity were slowly added dropwise to 25 ml of 0.045 M aqueous solution of ammonium fluoride. The resulted mother solution was aged on a magnetic stirrer for 60 minutes. After that, the particles were centrifuged and washed three times with deionized water. After the reaction and washing, the product had a pink color, the intensity of which increased with increasing concentration of the dopant. After synthesis annealing was carried out in quartz crucibles in air in a SNOL 6/12-B muffle furnace for 1 hour at a temperature of 650 °C. The choice of the maximum ErF_3 concentration in these types of compounds was limited by the formation of the single-phase solid solution, since when the ReF_3 content is more than 25 mol%, the probability of the formation of an impurity monoclinic phase along with the cubic one is high.^{32,33}

Nanosized crystals of $\text{ZrO}_{2-x} \text{ mol\% Er}_2\text{O}_3$ ($x = 5, 10, 15, 25$) were synthesized under hydrothermal conditions according to the procedure.³⁴ As starting reactants were used $\text{ZrO}(\text{NO}_3)_2 \cdot x\text{H}_2\text{O}$ (Sigma Aldrich, 99.99%) and $\text{Er}(\text{NO}_3)_3 \cdot 5\text{H}_2\text{O}$ (Acros Organic, 99.9%). All the reactants were analyzed to determine the amount of crystalhydrate water molecules and weighted up to the fourth decimal place. 27 ml of initial water solution with concentration of 0.06 M containing ions of zirconia and the dopant was precipitated with 23 ml of ammonia solution. The resulting suspension was subjected to hydrothermal treatment for 24 hours at a temperature of 200 °C. After the synthesis was complete the mother solution was titrated to prove that no metal ions were left. Absence of impurity phases in the samples proves that the expected amount of dopant has indeed entered the lattice. Yield of the reaction is quantities and the product is white in color. In order to increase the size of the obtained nanoparticles, they were additionally annealed in a muffle furnace at the first stage for 6 hours at a temperature of 800 °C and at the second stage for 6 hours at a temperature of 1200 °C.

The morphology of the synthesized $\text{CaF}_{2-x} \text{ mol\% ErF}_3$ and $\text{ZrO}_{2-x} \text{ mol\% Er}_2\text{O}_3$ particles was studied by scanning electron microscopy (SEM) on a three-beam Carl Zeiss NVision 40 workstation with the function of local energy dispersive X-ray analysis (EDX) and a transmission electron microscope (TEM) (Carl Zeiss Libra 200 MC).

X-ray diffraction was used for the phase analysis of the samples. It was carried out using an Empyrean PANalytical B.V. diffractometer ($\text{CuK}\alpha$ radiation, $\lambda = 1.5414 \text{ \AA}$) with a vertical goniometer and a PIXcel 3D detector (for $\text{CaF}_{2-x} \text{ mol\% ErF}_3$) and a Bruker D8 Advance diffractometer ($\text{CuK}\alpha$ radiation, Ni-filter and LYNXEYE detector, for $\text{ZrO}_{2-x} \text{ mol\% Er}_2\text{O}_3$). Phases were identified using database of International Centre for Diffraction Data (ICDD). Coherent scattering domain size was calculated with the help of Sherrer formula.

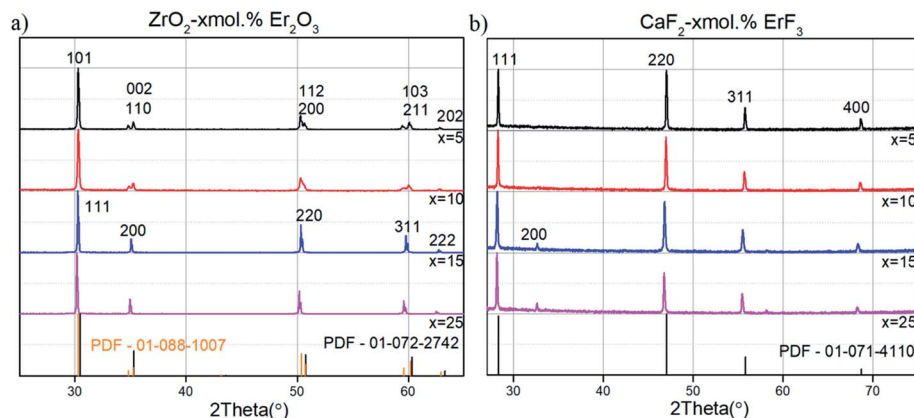


Fig. 1 XRD patterns of ZrO₂-x mol% Er₂O₃ (PDF-01-072-2742 – cubic phase;⁵⁵ PDF-01-088-1007 – tetragonal phase⁵⁶) (a) and CaF₂-x mol% ErF₃ (PDF-01-071-4110 – cubic phase⁵⁷) (b) (x = 5–25) concentration series.

Table 1 Lattice parameters (*a*, *c*), unit cell volume (*V*) and the micro-strain values (ϵ) of ZrO₂-x mol% Er₂O₃ and CaF₂-x mol% ErF₃ compositions

<i>x</i> , mol%	ZrO ₂ - <i>x</i> mol% Er ₂ O ₃			CaF ₂ - <i>x</i> mol% ErF ₃	
	<i>a</i> , Å	<i>c</i> , Å	<i>V</i> , Å ³	<i>a</i> , Å	<i>V</i> , Å ³
5	3.609	5.171	67.35	5.464	163.13
10	3.617	5.167	67.61	5.47	163.67
15	5.13		135.01	5.485	165.02
25	5.14		135.79	5.493	165.7

The lattice parameters were calculated using Topas R software (Bruker AXS, Karlsruhe, Germany) and HighScore Plus (PANalytical).

To record the diffuse reflectance spectra, suspensions consisting of nanopowders and silicate glue were applied to one side of the glass slides, the second side of the glass was covered with several layers of white paper. Diffuse reflectance spectra were measured with a 150 mm integrating sphere, which is an accessory to the Lambda 950 PerkinElmer spectrophotometer.

Spectral-luminescent studies were performed using an automated setup based on the MDR-23 monochromator. An Er-6.0 fiber erbium laser with $\lambda_{\text{exc}} = 1550$ nm was used as an excitation source. An FEU-79 photomultiplier was used as a radiation detector.

Images showing the color dynamics of the emission from the samples were obtained by extracting frames from a video (25

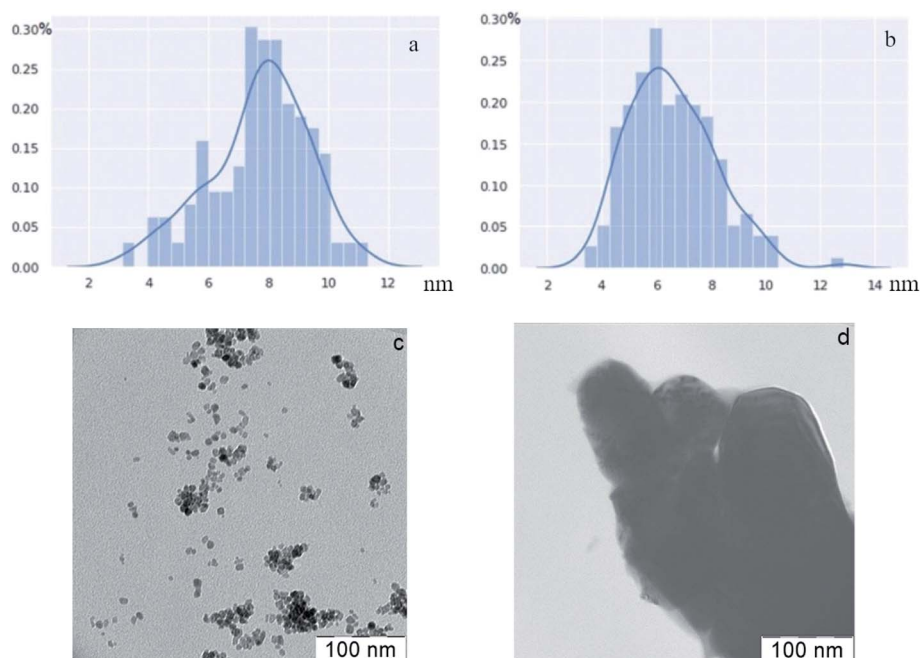


Fig. 2 Particle size distribution for samples of ZrO₂-x mol% Er₂O₃ (a) x = 5; (b) x = 25 pre-annealing. TEM-images of ZrO₂-x mol% Er₂O₃ (x = 5) before (c) and after (d) annealing at a temperature of 1200 °C.

frames per second) recorded using a Sony Nex F3K digital camera.

All measurements were carried out at room temperature.

3. Results and discussion

X-ray phase analysis of the CaF_2 - x mol% ErF_3 and ZrO_2 - x mol% Er_2O_3 ($x = 5$ –25) concentration series confirmed (Fig. 1) that both types of synthesized nanoparticles are single-phase and correspond to the structural type of cubic fluorite (sp. gr. $Fm\bar{3}m$) with the exception of the ZrO_2 - x mol% Er_2O_3 $x = 5, 10$ which had tetragonal structure (sp. gr. $P4_2/nmc$).¹⁰ Structural analysis of ZrO_2 - x mol% Er_2O_3 showed that lattice parameter monotonously increases as concentration of erbium grows (Table 1). The nonlinearity of the concentration–parameter relation is caused by the heterovalent nature of the substitution and vacancies formation induced by the presence of dopant ions.

The coherent scattering domain size (CSD) for all ZrO_2 - x mol% Er_2O_3 samples was estimated before annealing with the help of Sherrer formula. It can be noted that the CSD slowly decreases from 9 nm at 5 mol% to 5 nm at 25 mol% with dopant concentration increasing. This data is in agreement with the particle size distribution that is based on TEM photos (Fig. 2). SEM data (Fig. 3) shows that after the annealing the average particle size for ZrO_2 - x mol% Er_2O_3 ($x = 5, 10, 25$) corresponds to the range 100–200 nm and practically does not change in the selected range of Er_2O_3 concentrations. Particles with $x = 15$ have large sizes (~ 300 nm), which, apparently, is associated with annealing conditions. The particles consist of separate blocks average size of which was evaluated based on the CSD and turned out to be around 60–70 nm independently of erbium concentration. The microstrain values (ϵ) ranged from 2 to 6×10^{-4} .

Structural analysis of CaF_2 - x mol% ErF_3 also showed lattice parameter increasing with rise of erbium content (Table 1). Average CSD size was around 90 nm and the microstrain values (ϵ) ranged from 1 to 5×10^{-4} independently of erbium concentration. Analysis of the SEM-images of CaF_2 - x mol% ErF_3 samples ($x = 5, 10, 15, 25$) showed that the average nanoparticle size is about 200 nm and does not depend on the value of x (Fig. 4) with the exception of sample with $x = 15$ which average

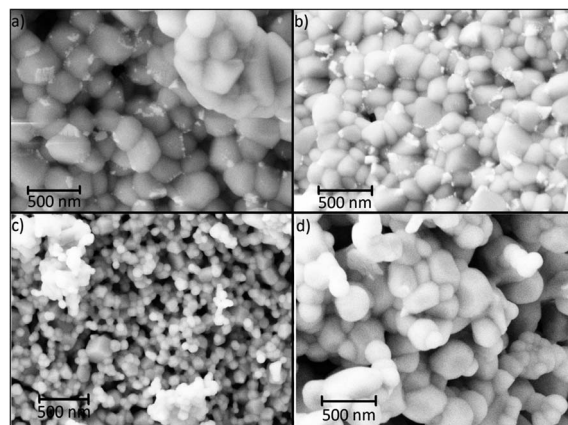


Fig. 4 SEM-images of CaF_2 - x mol% ErF_3 (a) $x = 5$; (b) $x = 10$; (c) $x = 15$; (d) $x = 25$.

particle size is smaller and equal to about 100 nm. Since in synthesis method the dropping of the chloride solution was carried out manually, a certain deviation of the particle sizes from the average is normal.

Thus, CaF_2 - x mol% ErF_3 and ZrO_2 - x mol% Er_2O_3 solid solutions are characterized by close values of the average particle size.

Excitation of CaF_2 - x mol% ErF_3 samples ($x = 5$ –25) to the $^4\text{I}_{13/2}$ level of Er^{3+} ions by continuous laser radiation with $\lambda_{\text{exc}} = 1550$ nm and power density $J = 0.15$ kW cm^{-2} led to upconversion luminescence of Er^{3+} ions due to transitions from excited levels of $^2\text{H}_{11/2}$, $^4\text{S}_{3/2}$, $^4\text{F}_{9/2}$, $^4\text{I}_{9/2}$ on the ground state $^4\text{I}_{15/2}$ of these ions. A similar luminescence was observed for samples with $x = 5$ –15 with an increase in J to 1.93 kW cm^{-2} (Fig. 5). In this case, the luminescence intensity ratio for the $^2\text{H}_{11/2} \rightarrow ^4\text{I}_{15/2}$, $^4\text{S}_{3/2} \rightarrow ^4\text{I}_{15/2}$ (500–570 nm) transitions and the $^4\text{F}_{9/2} \rightarrow ^4\text{I}_{15/2}$ transition (630–700 nm) increases with increasing erbium content in the sample ($x = 5$ –10). At $x = 15$, the relative line intensity decreases in the region of 500–570 nm, and a broad

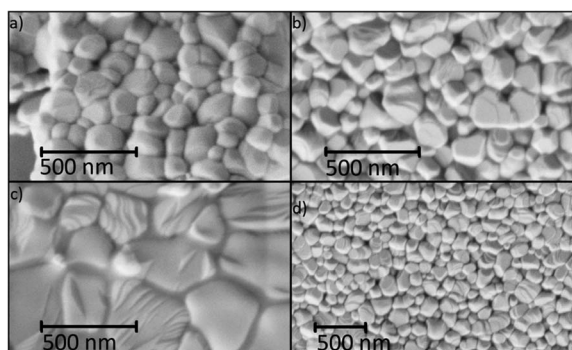


Fig. 3 SEM images of ZrO_2 - x mol% Er_2O_3 (a) $x = 5$; (b) $x = 10$ (c) $x = 15$; (d) $x = 25$.

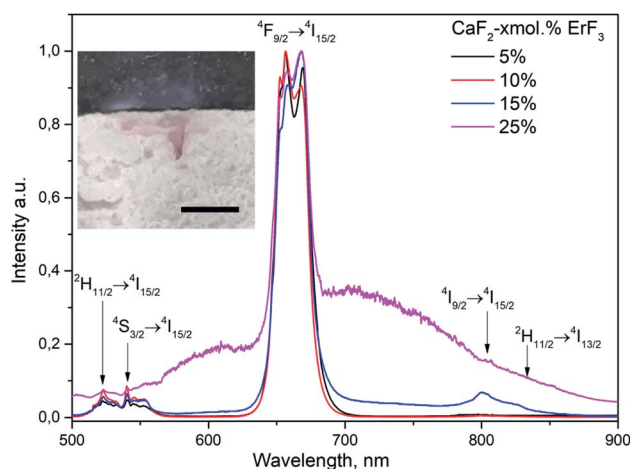


Fig. 5 Emission spectra of CaF_2 - x mol% ErF_3 ($x = 5$ –25), $\lambda_{\text{exc}} = 1550$ nm, $J = 1.93$ kW cm^{-2} . Photo on inset shows the trace of sample melting ($x = 5$) after arising BBE, scale bar corresponds to 2 mm.

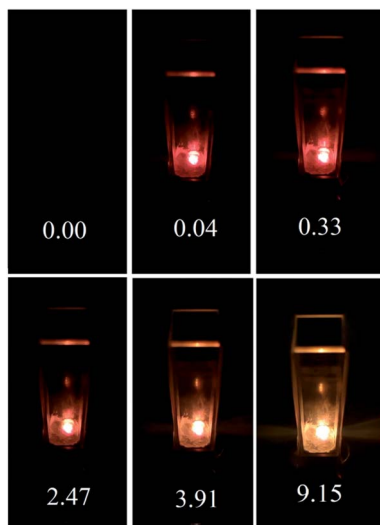


Fig. 6 Temporal dynamics of the emission color for a CaF_2 -25 mol% ErF_3 sample, $\lambda_{\text{exc}} = 1550$ nm, $J = 1.93$ kW cm^{-2} . The numbers in the figure indicate the time (in seconds) after turning on the laser.

band is observed in the region of 600–900 nm, which is not related to the luminescence of Er^{3+} ions. For the CaF_2 -25 mol% ErF_3 sample, BBE arises against the background of upconversion luminescence of Er^{3+} ions, and its relative intensity is lower than the intensity of the luminescence band of the ${}^4\text{F}_{9/2} \rightarrow {}^4\text{I}_{15/2}$ transition of Er^{3+} ions. The corresponding emission spectra of CaF_2 - x mol% ErF_3 samples ($x = 5$ –25) upon laser excitation with $J = 1.93$ kW cm^{-2} are presented in Fig. 5. For greater clarity, the spectra are presented without adjusting for the spectral sensitivity of the setup.

Since the morphology and particle sizes of CaF_2 - x mol% ErF_3 with $x = 25$, 10, and 5 are practically the same (Fig. 4), the main factor determining the differences in the emission spectra of these samples under identical excitation conditions (Fig. 5) is

the concentration of RE ions in them. The difference in the particle sizes of the sample with $x = 15$ did not lead to significant differences in its emission spectra from the spectra of samples with $x = 10$ and 5. Analysis of emission spectra for samples with $x = 5$ –25 can reveal small changes in the ratio of peak intensity for the main emission band (${}^4\text{F}_{9/2} \rightarrow {}^4\text{I}_{15/2}$). As mentioned in the introduction, the formation of RE ion clusters is characteristic of this type of compounds. In samples with different contents of RE ions, the cluster structure will have some differences, which, in turn, can lead to observed differences in spectra.

It should be noted that the buildup time of BBE in CaF_2 - x mol% ErF_3 ($x = 25$) to a maximum intensity is more than 9 seconds (Fig. 6), which significantly exceeds the buildup time (0.2 s) for ErPO_4 nanoparticles.⁸ In this case, at the initial stages after switching on the excitation source, a red glow was observed, which is characteristic of the luminescence of Er^{3+} ions due to the ${}^4\text{F}_{9/2} \rightarrow {}^4\text{I}_{15/2}$ transition. A similar character of buildup was noted earlier in ref. 5 and by us in ref. 7 and 8.

After correcting the BBE spectrum of the CaF_2 -25 mol% ErF_3 sample for instrumental response, the color temperature T_c of this emission was estimated using the method described in ref. 35 and was about 1800 K. It should be noted that regions with traces of melting were observed on the surface of the CaF_2 -25 mol% ErF_3 sample after exposure to laser radiation with $J = 1.93$ kW cm^{-2} . This indicates local heating of CaF_2 -25 mol% ErF_3 particles to the melting temperature (1691 K³⁶). In CaF_2 - x mol% ErF_3 ($x = 1$ –15) samples, no traces of melting were found after a same irradiation.

The study of the spectral and luminescent characteristics of ZrO_2 - x mol% Er_2O_3 ($x = 5$ –25) compounds revealed a number differences from the characteristics of CaF_2 - x mol% ErF_3 ($x = 1$ –25) under identical excitation conditions. Fig. 5 shows the emission spectra of ZrO_2 - x mol% Er_2O_3 ($x = 5$ –25), recorded upon excitation to the ${}^4\text{I}_{13/2}$ level of Er^{3+} ions by laser radiation with $\lambda_{\text{exc}} = 1550$ nm and $J = 0.89$ kW cm^{-2} .

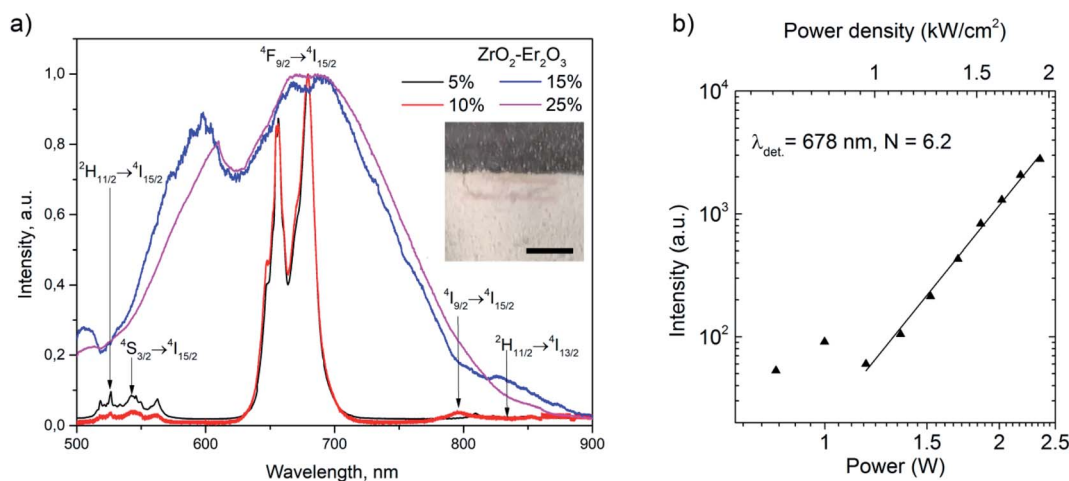


Fig. 7 Emission spectra of ZrO_2 - x mol% Er_2O_3 ($x = 5$, 10, 15, 25), $\lambda_{\text{exc}} = 1550$ nm, $J = 0.89$ kW cm^{-2} (a). Photo on inset shows the trace of sample melting ($x = 5$) after arising BBE, scale bar corresponds to 2 mm. Intensity of broadband radiation versus the pump power for ZrO_2 -25 mol% Er_2O_3 (b).

Fig. 7(a) demonstrates that, at the indicated J , upconversion luminescence of Er^{3+} ions is observed for samples with $x = 5, 10$, and intense BBE is observed for samples with $x = 15, 25$. The dip in the 600–650 nm region of the emission spectra of $\text{ZrO}_2-x \text{ mol\% Er}_2\text{O}_3$ ($x = 15, 25$) is associated with the features of the recording system, and the dips in the ranges of 500–550, 650–700 and 780–820 nm is due to the reabsorption of radiation by Er^{3+} ions. As J increases to 1.1 kW cm^{-2} , BBE is already detected in all $\text{ZrO}_2-x \text{ mol\% Er}_2\text{O}_3$ ($x = 5, 10, 15, 25$) samples. The $I(P)$ dependence for BBE in all samples is nonlinear and the slope is 5.8–6.2, as for the previously studied ErPO_4 powders.⁸ As an illustration, this dependence is presented for the $\text{ZrO}_2-25 \text{ mol\% Er}_2\text{O}_3$ sample in Fig. 7(b). As in the case of fluoride particles, the morphology and particle sizes of $\text{ZrO}_2-x \text{ mol\% Er}_2\text{O}_3$ with $x = 25, 10$, and 5 do not differ significantly (Fig. 3), which allows us to relate the differences in the behavior of the emission spectra of these samples (under identical excitation conditions) with different RE ions content in them. As noted in the manuscript, the particle size of the sample with $x = 15$ is slightly different from the rest of the samples, however, its spectral-luminescent properties are close to the properties of the sample with $x = 25$ (Fig. 7).

The buildup character of BBWE in $\text{ZrO}_2-x \text{ mol\% Er}_2\text{O}_3$ ($x = 5, 10, 15, 25$) compounds is also similar to that observed in $\text{Y}_{0.95(1-x)}\text{Yb}_{0.95x}\text{Er}_{0.05}\text{PO}_4$, $\text{Y}_{0.95(1-x)}\text{Yb}_{0.95x}\text{Er}_{0.05}\text{PO}_4 \cdot 0.8\text{H}_2\text{O}$ nanopowders and is described in ref. 7 and 24. As an illustration, Fig. 8 shows the temporal dynamics of the emission color of the $\text{ZrO}_2-5 \text{ mol\% Er}_2\text{O}_3$ sample, the numbers in the figure indicate the time (in seconds) after the laser was turned on.

It can be seen that, at the initial moment after switching on the excitation source with $J = 1.1 \text{ kW cm}^{-2}$, up-conversion luminescence of Er^{3+} ions is observed in nanoscale crystalline powders $\text{ZrO}_2-5 \text{ mol\% Er}_2\text{O}_3$. BBE in these compounds appears 0.23 s after switching on the excitation source, and reaches a maximum intensity in 3.6 s, which is almost three times faster than in $\text{CaF}_2-25 \text{ mol\% ErF}_3$.

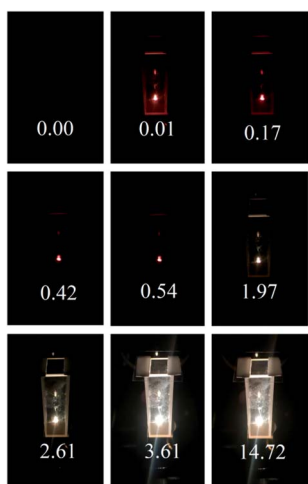


Fig. 8 Temporal dynamics of the emission color for a $\text{ZrO}_2-5 \text{ mol\% Er}_2\text{O}_3$ sample, $\lambda_{\text{exc}} = 1550 \text{ nm}$, $J = 1.1 \text{ kW cm}^{-2}$. The numbers indicate the time (in seconds) after the laser was turned on.

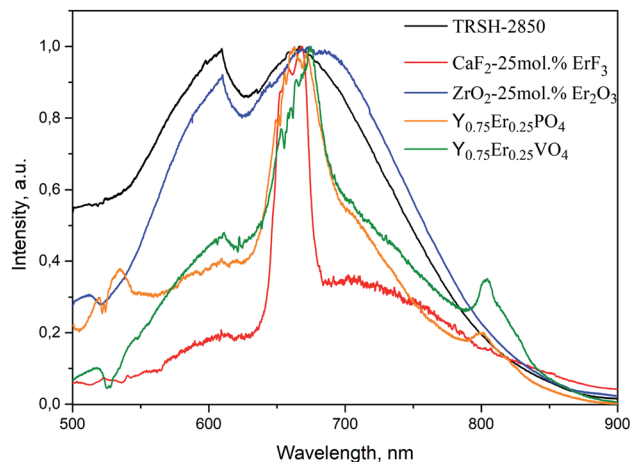


Fig. 9 Emission spectra of $\text{CaF}_2-25 \text{ mol\% ErF}_3$ ($J = 1.93 \text{ kW cm}^{-2}$), $\text{ZrO}_2-25 \text{ mol\% Er}_2\text{O}_3$ ($J = 0.89 \text{ kW cm}^{-2}$), $\text{Y}_{0.75}\text{Er}_{0.25}\text{PO}_4$ ($J = 1.39 \text{ kW cm}^{-2}$),⁸ $\text{Y}_{0.75}\text{Er}_{0.25}\text{VO}_4$ ($J = 0.52 \text{ kW cm}^{-2}$)⁸ ($\lambda_{\text{exc}} = 1550 \text{ nm}$), and the TRSH-2850 tungsten lamp.

After correction the BBE spectra of the $\text{ZrO}_2-x \text{ mol\% Er}_2\text{O}_3$ ($x = 5, 10, 15, 25$) concentration series for J equal to 0.89, 1.45, 1.93 kW cm^{-2} , we estimated the emission color temperatures T_c , which corresponded to the range of 2200–2720 K.

A comparison of BBE spectra of $\text{ZrO}_2-x \text{ mol\% Er}_2\text{O}_3$ and the spectrum of the tungsten lamp (color temperature of 2850 K) revealed similarity of their forms. As an illustration, Fig. 9 shows the emission spectra of $\text{CaF}_2-25 \text{ mol\% ErF}_3$, $\text{ZrO}_2-25 \text{ mol\% Er}_2\text{O}_3$ samples and the TRSH-2850 tungsten lamp, as well as the spectra of $\text{Y}_{0.75}\text{Er}_{0.25}\text{PO}_4$ and $\text{Y}_{0.75}\text{Er}_{0.25}\text{VO}_4$ (ref. 8) particles without correction for instrumental response.

As noted above, in ref. 7 and 8 we presented an occurrence mechanism of blackbody emission in nanoscale orthophosphate and orthovanadate dielectric particles doped with RE ions. This mechanism includes a number of processes (Fig. 10). When nanoparticles are excited by laser radiation with a high

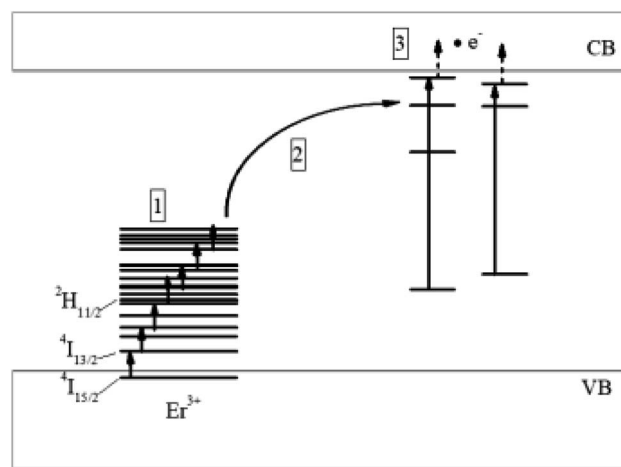


Fig. 10 Scheme of the processes leading to the appearance of thermal emission in nanoscale $\text{ZrO}_2-x \text{ mol\% Er}_2\text{O}_3$ and $\text{CaF}_2-x \text{ mol\% ErF}_3$ crystals under laser excitation ($\lambda_{\text{exc}} = 1550 \text{ nm}$).

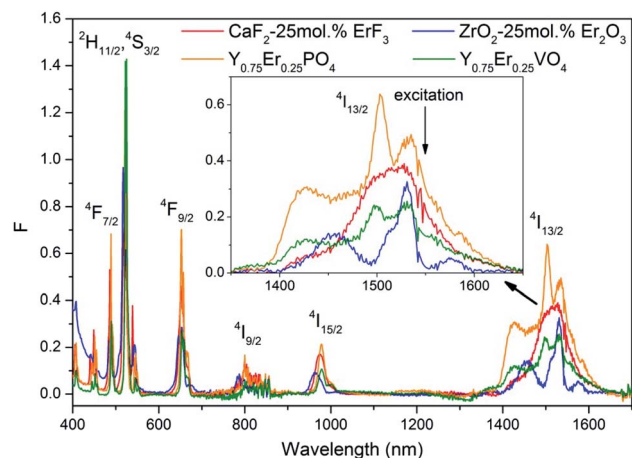


Fig. 11 Diffuse reflection spectra of CaF_2 -25 mol% ErF_3 , ZrO_2 -25 mol% Er_2O_3 , $\text{Y}_{0.75}\text{Er}_{0.25}\text{PO}_4$, $\text{Y}_{0.75}\text{Er}_{0.25}\text{VO}_4$.

power density to the absorption band of the RE ions, nonlinear interaction of these ions occurs and leads to population of their high energy levels (1). Further, ions excited to high energy levels interact with defects in the crystal structure (2), for example, with surface defects. Then, the electrons pass from the energy levels of defects into the conduction band and their interaction with the lattice phonons (3) results to the nanoparticle heating, which, in turn, leads to the BBWE appearance. An analysis of the characteristics of this emission for the ZrO_2 - x mol% Er_2O_3 and CaF_2 - x mol% ErF_3 particles studied in this work allows us to conclude that the our proposed mechanism is also applicable to these particles.

Now we analyze the effect of some physical characteristics and geometric factors of CaF_2 -25 mol% ErF_3 , ZrO_2 -25 mol% Er_2O_3 , $\text{Y}_{0.75}\text{Er}_{0.25}\text{PO}_4$,⁸ $\text{Y}_{0.75}\text{Er}_{0.25}\text{VO}_4$ (ref. 8) nanoparticles on the conditions of the BBE appearance in them and its characteristics.

Since BBWE is observed in dielectric particles doped with RE ions when they are excited by laser radiation of a certain intensity in the absorption bands of these ions, the conditions for its occurrence may depend on the absorption and scattering coefficients of the radiation at an excitation wavelength. However, evaluative studies using diffuse optical spectroscopy revealed that there are no cardinal differences at the excitation wavelength in the absorption spectra of CaF_2 -25 mol% ErF_3 , ZrO_2 -25 mol% Er_2O_3 , $\text{Y}_{0.75}\text{Er}_{0.25}\text{PO}_4$, $\text{Y}_{0.75}\text{Er}_{0.25}\text{VO}_4$ samples. As confirmation, Fig. 11 shows the diffuse reflection spectra of these samples converted using the Kubelka–Munk formula.³⁷

The next feature of nanoparticles, which can affect their spectral and luminescent properties, is a high surface to volume ratio.³⁸ This feature leads to an increase in the fraction of near-surface RE ions with an environment different from the environment of ions inside the particle. However, for our studied particle size range, such an effect will be insignificant.³⁹ As noted above, the average particle sizes of CaF_2 -25 mol% ErF_3 are 200 nm, ZrO_2 -25 mol% Er_2O_3 are 100–200 nm, and the particle sizes of $\text{Y}_{0.75}\text{Er}_{0.25}\text{PO}_4$ and $\text{Y}_{0.75}\text{Er}_{0.25}\text{VO}_4$ correspond to ranges 20–50 and 40–100 nm.⁸

In ref. 8, we also suggested that the material band gap (E_g) affects the appearance of thermal emission. The band gap affects the number of transitions that an electron must undergo in order to get into the conduction band. In order to be at the high energy level corresponding to the energy level of the structural defect, the electron will need to overcome a larger number of transitions in a compound with large E_g than in a compound with a smaller E_g . For clarity, Table 2 shows the band gap values (E_g) and melting temperatures (T_m) of the materials, the threshold power density of the exciting radiation (J_{thr}), as well as BBE color temperatures (T_c). The threshold power density of the exciting radiation (J_{thr}) was estimated from the $I(P)$ dependence.

The table shows that the smallest J_{thr} value corresponds to $\text{Y}_{0.75}\text{Er}_{0.25}\text{VO}_4$ with the narrowest band gap. As noted in ref. 8, with a further increase in J , the BBE arising in these materials became unstable. This fact, apparently, is associated with the particle recrystallization as a result of significant heating in the region of BBE occurrence. With increasing E_g , the value of J also increases.

Excitation of compounds with RE ions can lead not only to luminescence of these ions, but also to nonradiative relaxation processes, which will lead to additional heating of the samples. As noted in the introduction, some authors^{12,31} attribute the occurrence of thermal “white” emission precisely to these processes. In our case, when erbium-containing nanoparticles are excited to the $^4\text{I}_{13/2}$ level of Er^{3+} ions, the probability of nonradiative relaxation from this level to the $^4\text{I}_{15/2}$ ground state is close to zero, since the energy gap between these levels (6500 cm^{-1}) is several times higher than vibrational quantum ν (Table 2). Excitation of Er^{3+} ions to the $^4\text{I}_{13/2}$ level also leads to population of higher levels, the probability of nonradiative relaxation from which is nonzero. In ref. 8, we directly excited to one of these levels ($^2\text{H}_{11/2}$), but no BBE was observed. This allowed us to conclude that nonradiative relaxation does not play a major role in its appearance. If nonradiative relaxation from excited levels of RE ions played a significant role in

Table 2 Parameters of BBE in different studied matrices

Compound	E_g , eV	J_{thr} , kW cm^{-2}	T_c , K	T_m , K	ν , cm^{-1}
CaF_2 -25 mol% ErF_3	12 (ref. 19)	1.93	1800	1691 (ref. 36)	443 (ref. 40)
$\text{Y}_{0.75}\text{Er}_{0.25}\text{PO}_4$	8.6–9.2 (ref. 15 and 16)	1.39 (ref. 8)	2400 (ref. 8)	2173 (ref. 41)	1061 (ref. 42)
ZrO_2 -25 mol% Er_2O_3	4.6–4.7, ^{28,29} 5.49–5.8 (ref. 27 and 30)	0.89	2200	2973 (ref. 43)	625 (ref. 44)
$\text{Y}_{0.75}\text{Er}_{0.25}\text{VO}_4$	3.4–3.8 (ref. 17 and 18)	0.52 (ref. 8)	1800 (ref. 8)	2083 (ref. 45)	891 (ref. 20)

increasing the temperature of the samples, then thermal emission would be most pronounced for compounds with a large value of ν and would be less pronounced for materials with small ν . However, as follows from Table 2, despite the fact that ν values for ZrO_2 -25 mol% Er_2O_3 and $\text{Y}_{0.75}\text{Er}_{0.25}\text{PO}_4$ are two times different, the BBWE color temperatures in these compounds are close. Apparently, the presence of defects in the crystal structure, in particular, oxygen vacancies, is a more important factor affecting the conditions for the appearance of BBE in ZrO_2 - x mol% Er_2O_3 nanopowders.

The influence of defects on the conditions for the appearance of thermal emission is clearly seen in the analysis of its features in ZrO_2 -25 mol% Er_2O_3 nanoparticles. Fig. 7 shows that the BBWE in ZrO_2 -25 mol% Er_2O_3 has the highest relative intensity, while in CaF_2 -25 mol% ErF_3 , $\text{Y}_{1-x}\text{Er}_x\text{PO}_4$, $\text{Y}_{(1-x)}\text{Er}_x\text{VO}_4$ ($x = 0.25$) it has a background character. Moreover, the considered emission appeared in ZrO_2 - x mol% Er_2O_3 even at low x values (5, 10), which was not observed for other samples in the available range of J . As noted in the introduction, heterovalent substitution of Zr^{4+} ions by Er^{3+} ions leads to the appearance of oxygen vacancies in ZrO_2 - M_2O_3 , structural defects, which are characterized by energy levels near the conduction band.^{27–30,46,47} According to studies, the energy levels of oxygen vacancy is located at 2.5–2.6 eV (19 600–20 300 cm^{-1}), 3.3–3.8 eV (\sim 25 800–29 700 cm^{-1}) and 4–5 eV (\sim 31 200–39 000 cm^{-1}).^{27,28,47} X-ray phase analysis of the ZrO_2 - x mol% Er_2O_3 ($x = 5$ –25) concentration series confirmed (Fig. 1) that synthesized nanoparticles are single-phase and correspond to the structural types which are typical for ZrO_2 - M_2O_3 compounds with similar RE content. Consequently, the synthesized compound will possess typical features for this structure, in particular, it will be characterized by the presence of defects. The presence of a significant number of such defects ZrO_2 -25 mol% Er_2O_3 and their interaction with Er^{3+} ions excited to high energy levels will greatly contribute to the appearance of electrons in the conduction band.

It should be noted that an important role in the population of the upper energy levels of Er^{3+} ions is played by the resonances in the energy level system, as well as the interaction probability of ions with each other. This probability increases with decreasing distance between ions and with increasing their concentration. In addition, the interaction processes will proceed more intensively with an increase in the excitation power density. The effective interaction of Er^{3+} ions in all samples studied both in this work and earlier⁸ is evidenced by the presence of upconversion luminescence of these ions. Also, a clear dependence of the BBWE occurrence on the RE ions content is observed for all the studied samples. This is due to the fact that, at low concentrations of these ions, the processes of interaction between them and with defects are not intense enough to transfer a significant number of electrons into the conduction band. In CaF_2 - x mol% ErF_3 compounds, the described interaction will be more effective due to the clustering of RE ions.^{21,22} Nevertheless, according to the results presented above, the process of the appearance of BBWE in these compounds is less pronounced in comparison with other

compounds. This fact is an additional confirmation that the value of E_g is a significant factor.

To summarize, we can list the main factors affecting the conditions for the BBE appearance in dielectric nanoparticles doped with RE ions when they are excited by intense laser radiation. These include the band gap of the material and the presence of defects in its crystal structure. Also, one cannot exclude the effect of the RE ions absorption at the excitation wavelength.

The obtained results are not only of fundamental importance, but can also be used in practice, for example, in dermatology, to remove skin neoplasms. Currently, infrared (IR) lasers are the most common in this area, and their radiation is delivered to the tissue *via* optical fiber, which allows both contactless and contact effects on biological tissue to be realized.^{48–54} To increase the thermal effect during contact exposure and increase the efficiency of the procedure, “blackening” of the fiber end face is proposed.⁵¹ Such a modification does not provide for the reuse of fiber and increases the cost of the procedure. Coating the biological tissue with ZrO_2 - x mol% Er_2O_3 nanoparticles, which are bioinert, can act as an alternative way of enhancing the thermal effect of the contactless IR irradiation. This method will also allow the use of radiation sources with a relatively low power (\sim 1–2 W), which will positively affect the cost of the procedure.

4. Conclusion

In this work, we studied the features of broadband “white” emission in CaF_2 - x mol% ErF_3 and ZrO_2 - x mol% Er_2O_3 nanoparticles upon their excitation by laser radiation with $\lambda_{\text{exc}} = 1550$ nm. In CaF_2 - x mol% ErF_3 nanoparticles, this emission arose at an erbium concentration of 25 mol% and an excitation power density J equal to 1.93 kW cm^{-2} and had a background character with respect to the luminescence bands of Er^{3+} ions due to ${}^2\text{H}_{11/2}$, ${}^4\text{S}_{3/2}$, ${}^4\text{F}_{9/2}$, ${}^4\text{I}_{9/2}$ transitions to the ground state ${}^4\text{I}_{15/2}$ of these ions. In ZrO_2 - x mol% Er_2O_3 nanoparticles (15, 25), the indicated emission was observed at a lower value of J (0.89 kW cm^{-2}), and when J increased to 1.1 kW cm^{-2} , it also appeared in samples with $x = 5, 10$.

Comparison of the results obtained in this study with those obtained earlier for erbium-containing particles of orthophosphates and orthovanadates,⁸ confirmed the nature and the mechanism of the appearance of “white” emission that we proposed. We have revealed the dependence of the threshold excitation power density necessary for its appearance on the band gap of the material and found that this parameter is one of the dominant ones. Also, by the example of ZrO_2 - x mol% Er_2O_3 nanoparticles, it was demonstrated that the presence of crystal structure defects is the next key factor contributing to the appearance of thermal emission.

Conflicts of interest

There are no conflicts to declare.

Acknowledgements

This work was supported by the Russian Foundation for Basic Research (grant number 19-32-90135), the Ministry of Science and Higher Education within the State assignment FSRC “Crystallography and Photonics” RAS in part of electron microscopy.

References

- 1 S. M. Redmond, S. C. Rand and S. L. Oliveira, *Appl. Phys. Lett.*, 2004, **85**, 5517.
- 2 L. Marciniak, W. Strek, D. Hreniak and Y. Guyot, *Appl. Phys. Lett.*, 2014, **105**, 173113.
- 3 W. Strek, L. Marciniak, A. Bednarkiewicz, A. Lukowiak, R. Wiglusz and D. Hreniak, *Opt. Express*, 2011, **19**, 14084.
- 4 J. Wang and P. A. Tanner, *J. Am. Chem. Soc.*, 2010, **132**, 947.
- 5 S. Redmond, S. C. Rand, X. L. Ruan and M. Kaviany, *J. Appl. Phys.*, 2004, **95**, 4069.
- 6 J.-F. Bisson, D. Kouznetsov, K.-I. Ueda, S. T. Fredrich-Thornton, K. Petermann and G. Huber, *Appl. Phys. Lett.*, 2007, **90**, 201901.
- 7 S. A. Khrushchalina, P. A. Ryabochkina, V. M. Kyashkin, A. S. Vanetsev, O. M. Gaytko and N. Yu Tabachkova, *JETP Lett.*, 2016, **103**, 302–308.
- 8 S. A. Khrushchalina, P. A. Ryabochkina, M. N. Zharkov, V. M. Kyashkin, N. Y. Tabachkova and I. A. Yurlov, *J. Lumin.*, 2019, **205**, 560–567.
- 9 A. V. Egorysheva, O. M. Gajtko, S. V. Golodukhina, S. A. Khrushchalina, P. A. Ryabochkina, A. D. Taratynova and I. A. Yurlov, *Ceram. Int.*, 2019, **45**, 16886–16892.
- 10 Y. Hikichi, T. Sasaki, K. Murayama, T. Nomura and M. Miyamoto, *J. Am. Ceram. Soc.*, 1989, **72**, 1073.
- 11 M. R. N. Soares, M. Ferro, F. M. Costa and T. Monteiro, *Nanoscale*, 2015, **7**(47), 19958–19969.
- 12 J. Wang, T. Ming, Z. Jin, J. Wang, L.-D. Sun and C.-H. Yan, *Nat. Commun.*, 2014, **5**(1), 1–8.
- 13 S. Tabanlı, H. Cinkaya Yilmaz, G. Bilir, M. Erdem, G. Eryurek, B. Di Bartolo and J. Collinse, *ECS J. Solid State Sci. Technol.*, 2018, **7**(1), 3199–3210.
- 14 C. I. Silva Filho, A. L. Oliveira, S. C. F. Pereira, G. F. de Sá, L. L. da Luz and S. Alves Júnior, *Dalton Trans.*, 2018, **48**(8), 2574–2581.
- 15 W. Da-Wei, H. Shi-Hua, Y. Fang-Tian and T. Ye, *Chin. Phys. C*, 2009, **33**, 1019–1022.
- 16 J. J. Bos, P. Dorenbos, A. Bessière and B. Viana, *Radiat. Meas.*, 2008, **43**, 222–226.
- 17 A. H. Krumpel, E. van der Kolk, E. Cavalli, P. Boutinaud, M. Bettinelli and P. Dorenbos, *J. Phys.: Condens. Matter*, 2009, **21**, 115503.
- 18 Y. Fujimoto, T. Yanagida, Y. Yokota, V. Chani, V. V. Kochurikhin and A. Yoshikawa, *Nucl. Instrum. Methods Phys. Res., Sect. A*, 2011, **635**, 53–56.
- 19 H. Shi, R. I. Eglitis and G. Borstel, *Phys. Rev.*, 2005, **72**, 045109.
- 20 S. A. Miller, H. H. Caspers and H. E. Rast, *Phys. Rev.*, 1968, **168**, 964.
- 21 B. P. Sobolev, A. M. Golubev and P. Herrero, *Crystallogr. Rep.*, 2003, **48**(1), 141–161.
- 22 S. A. Kazanskiĭ, *JETP Lett.*, 1983, **38**, 521.
- 23 N. I. Sorokin and B. P. Sobolev, *Phys. Solid State*, 2019, **61**, 2034.
- 24 P. A. Ryabochkina, S. A. Khrushchalina, V. M. Kyashkin, A. S. Vanetsev, O. M. Gaytko and N. Yu Tabachkova, *JETP Lett.*, 2016, **103**, 743–751.
- 25 F. Auzel, *Chem. Rev.*, 2004, **104**, 139.
- 26 L. Marciniak, R. Tomala, M. Stefanski, D. Hreniak and W. Strek, *J. Rare Earths*, 2016, **34**, 227–234.
- 27 N. Nicoloso, A. Löbert and B. Leibold, *Sens. Actuators, B*, 1992, **8**(3), 253–256.
- 28 E. D. Wachsman, N. Jiang, C. W. Frank, D. M. Mason and D. A. Stevenson, *Appl. Phys. A: Solids Surf.*, 1990, **50**(6), 545–549.
- 29 V. R. PaiVerneker, A. N. Petelin, F. J. Crowne and D. C. Nagle, *Phys. Rev. B: Condens. Matter Mater. Phys.*, 1989, **40**(12), 8555–8557.
- 30 C. Ricca, A. Ringuedé, M. Cassir, C. Adamoa and F. Labat, *RSC Adv.*, 2015, **5**, 13941–13951.
- 31 F. González, R. Khadka, R. López-Juárez, J. Collins and B. Di Bartolo, *J. Lumin.*, 2018, **198**, 320–326.
- 32 B. P. Sobolev, *The Rare Earth Trifluorides. Part 1. The High Temperature Chemistry of the Rare Earth Trifluorides*, ed. B. P. Sobolev, Barcelona: Institut d'Estudis Catalans, 2000, p. 530, ISBN 84-7283-518-9.
- 33 P. P. Fedorov and B. P. Sobolev, *J. Less-Common Met.*, 1979, **63**(1), 31–43.
- 34 V. O. Veselova, I. A. Yurlov, P. A. Ryabochkina and A. V. Egorysheva, *Russ. J. Inorg. Chem.*, 2020, **65**, in press.
- 35 A. N. Magunov, *Instrum. Exp. Tech.*, 2009, **52**, 451–472.
- 36 P. A. Popov, P. P. Fedorov and V. V. Osiko, *Phys. Solid State*, 2010, **52**, 504–508.
- 37 G. Kortüm and J. Vogel, *Z. Phys. Chem.*, 1958, **18**, 230.
- 38 P. C. S. Filho and O. A. Serra, *J. Phys. Chem.*, 2011, **115**, 636.
- 39 H.-D. Nguyen, S.-i. Mho and I.-H. Yeo, *J. Lumin.*, 2009, **129**, 1754–1758.
- 40 K. Tahvildari, M. Esmaeilipour, S. Ghammamy and H. Nabipour, *Int. J. Nano Dimens.*, 2012, **2**(4), 269–273.
- 41 Y. Hikichi and T. Nomura, *J. Am. Ceram. Soc.*, 1987, **70**, 252.
- 42 G. M. Begun, G. W. Beall, L. A. Boatner and W. J. Gregor, *J. Raman Spectrosc.*, 1984, **11**, 273–278.
- 43 V. V. Osiko, M. A. Borik and E. E. Lomonova, *Technique Springer Handbook of crystal growth*, 2010, ch. 14, vol. 353, pp. 432–477.
- 44 C. M. Phillippi and K. S. Mazdiasni, *J. Am. Ceram. Soc.*, 1971, **54**(5), 254–258.
- 45 E. M. Levin, *J. Am. Ceram. Soc.*, 1967, **50**(7), 381–382.
- 46 X. Li, X. Mao, M. Feng, J. Xie, B. Jiang and L. Zhang, *J. Eur. Ceram. Soc.*, 2016, **36**(16), 4181–4184.
- 47 A. S. Foster, V. B. Sulimov, F. Lopez Gejo, A. L. Shluger and R. M. Nieminen, *Phys. Rev. B: Condens. Matter Mater. Phys.*, 2001, **64**, 224108.
- 48 A. Klein, W. B. Umler, M. Landthaler and P. Babilas, *Int. J. Hyperthermia*, 2011, **27**(8), 762–770.

- 49 B. Azadgoli and R. Y. Baker, *Ann. Transl. Med.*, 2016, **4**(23), 452.
- 50 J. N. Pozner and B. E. DiBernardo, *Clin. Plast. Surg.*, 2016, **43**(3), 515–525.
- 51 A. V. Belikov, M. L. Gelfond, K. V. Shatilova, S. A. Sosenkova and A. A. Lazareva, *Proc. of SPIE-OSA Biomedical Optics*, 2015, vol. 9542, p. 95420.
- 52 W. G. Stebbins, C. W. Hanke and J. Petersen, *Dermatol. Ther.*, 2011, **24**, 125–130.
- 53 A. N. Kassab and A. E. Kharbotly, *Eur. Arch. Oto-Rhino-Laryngol.*, 2012, **269**, 419–423.
- 54 U. Wollina, *Indian J. Dermatol.*, 2016, **61**(5), 540–544.
- 55 G. Katz, *J. Am. Ceram. Soc.*, 1971, **54**, 531.
- 56 J. Malek, L. Benes and T. Mitsuhashi, *Powder Diffr.*, 1997, **12**, 96.
- 57 H. E. Swanson and E. Tatge, *Natl. Bur. Stand. Circ.*, 1953, **539**, 69.